Sound & Vibration 2025, 59(5), 3676.
doi: https://doi.org/10.59400/sv3676

Article

Research on low-frequency sound insulation characteristics of metamaterials based on coupling of local resonance and Helmholtz resonators

Wenmin Zhang[1], Shangshuai Jia[1], Xinli Zhao[1], Lixin Zheng[2], Cai Zeng[3,*]

[1] CRRC Tangshan Co., Ltd., Tangshan 064099, China

[2] State Key Laboratory of Rail Transit Vehicle System, Southwest Jiaotong University, Chengdu 610031, China

[3] School of Electrical Engineering, Southwest Jiaotong University, Chengdu 610031, China

*** Corresponding author:** Cai Zeng, zengc0605@163.com

CITATION

Zhang W, Jia S, Zhao X, et al. Research on low-frequency sound insulation characteristics of metamaterials based on coupling of local resonance and Helmholtz resonators. Sound & Vibration. 2025; 59(5): 3676. https://doi.org/10.59400/sv3676

ARTICLE INFO

Received: 12 August 2025
Revised: 7 September 2025
Accepted: 11 October 2025
Available online: 29 October 2025

Abstract: This study addresses the challenge of low-frequency noise control by proposing a novel composite acoustic metamaterial that synergistically couples a multilayer locally resonant acoustic metamaterial (MLRAM) with a dual-cavity Helmholtz resonator. The research systematically investigates the sound insulation performance through an integrated approach combining theoretical analysis, finite element simulation, and impedance tube experimentation. Results demonstrate that while the MLRAM structure generates a significant sound insulation peak of 44.5 dB at 214 Hz, it is accompanied by a pronounced insulation valley of 6.4 dB at 228 Hz. To mitigate this limitation, a dual-cavity Helmholtz resonator was designed, achieving near-perfect absorption ($\alpha > 0.99$) and corresponding insulation peaks at 236 Hz and 316 Hz. The integrated composite structure effectively elevates the original insulation valley by 3.0 dB and introduces a new insulation peak of 32.0 dB at 311 Hz. Parametric studies reveal that the resonance frequencies can be precisely tuned by adjusting the neck geometry, and increasing the number of cavities broadens the effective bandwidth at the expense of peak amplitude. After optimization, the composite structure achieves a remarkable valley improvement of up to 10.8 dB and an average sound transmission loss of 21.0 dB, significantly enhancing broadband low-frequency sound insulation performance. This work provides a validated strategy for active "valley compensation" in acoustic metamaterials.

Keywords: acoustic metamaterials; local resonance; Helmholtz resonator; impedance tube testing

1. Introduction

Vibration and noise control is a classic challenge in the field of engineering, and it is particularly problematic in the low-frequency range (< 400 Hz). Vibration and noise are prevalent in scenarios such as transportation, construction, and mechanical equipment operation. They not only accelerate equipment wear and increase energy consumption but may also trigger structural damage and other safety hazards. Simultaneously, noise pollution accompanying vibration can harm human health (e.g., hearing impairment and psychological stress) and negatively impact the ecological environment. Therefore, effective control of vibration and noise has become a critical issue in the modernization process [1].

In recent years, acoustic metamaterials have garnered widespread attention as novel materials for vibration and noise reduction [2]. These artificially engineered

periodic composite materials exhibit diverse structural forms through unit cell design and periodic arrangement. Locally resonant metamaterials possess unique acoustic properties such as negative effective mass density [3] and negative effective modulus [4]. Their bandgap characteristics enable "small-scale control of large wavelengths," demonstrating excellent performance in the low-frequency range. Consequently, leveraging the unique acoustic properties of acoustic metamaterial structures to enhance the vibration and noise reduction performance of panels at low frequencies, and exploring their application prospects in practical engineering, holds significant importance for improving the operational efficiency and service life of various large-scale equipment and reducing environmental noise pollution [5]. Among them, locally resonant acoustic metamaterials and Helmholtz resonator-based acoustic metamaterials are currently two types of metamaterials with superior noise reduction effects.

Locally resonant acoustic metamaterials can achieve low-frequency vibration reduction with compact structures through their unique bandgap characteristics, breaking the mass law limitation of traditional sound insulation components [6]. By adjusting geometric and material parameters, these materials can exhibit special properties such as negative mass density and negative elastic modulus, and precisely control bandgap characteristics, providing innovative solutions for engineering vibration and noise control. Janssen et al. [7] proposed a design framework based on lumped parameter and finite element model optimization, and designed a metamaterial panel with multiple resonant units. Oudich et al. [8] discovered through COMSOL simulations that the Lamb wave bandgap characteristics of similar structures are significantly influenced by pillar height and cross-sectional area. Subsequent experiments validated the application potential of this structure in vibration and noise control [9]. Xiao et al. [10] demonstrated that metamaterial plates with spring-mass resonator arrays exhibit superior sound transmission loss in specific frequency bands compared to conventional plates and significantly enhance sound insulation performance in the coincidence region. Ho et al. [11] developed a multilayer locally resonant acoustic barrier panel, achieving excellent sound insulation in the 200–500 Hz low-frequency range by tuning resonance frequencies. Existing studies have demonstrated that a single locally resonant structure can generate one sound insulation peak and one sound insulation valley within a specific frequency band. When multiple locally resonant structures are combined or a single locally resonant structure incorporates multiple oscillators, multiple peaks and troughs can be achieved, which can be used to improve the sound insulation performance of the structure. Naify et al. [12, 13] showed that the use of multiple ring masses or multiple metamaterial units can yield sound transmission loss (STL) with multiple peaks. Zhang et al. [14] and Wang et al. [15] adopted a similar approach: by adding different additional masses to different cells of the metamaterial plate, they constructed various vibration responses, thereby achieving broadband sound insulation. Although locally resonant metamaterial structures can produce sound insulation peaks within the bandgap frequency range, a sound insulation valley with a sound insulation capacity far below the mass law appears after the peaks. Meanwhile, the sound insulation effect

in subsequent frequency bands is also weaker than that predicted by the mass law, which impairs the overall sound insulation performance of the structure. Therefore, in recent years, research on locally resonant metamaterials by experts and scholars has been focused on broadening the effective sound insulation frequency band at low frequencies and improving the sound insulation valleys.

Meanwhile, Helmholtz resonators exhibit excellent sound absorption performance at their resonant frequencies [16–19]. A Helmholtz resonator consists of a neck tube and a cavity, and its working principle can be simplified to a spring-mass model. When the frequency of the incident acoustic wave matches the natural frequency of the structure, the air column in the neck tube (acting as the mass) resonates with the air in the cavity (acting as the spring), converting acoustic energy into thermal energy via the viscous effect. This mechanism enables the resonator to achieve superior sound absorption performance at specific frequencies [17]. In recent years, research on optimizing Helmholtz resonators has primarily focused on enhancing absorption coefficients and broadening frequency bands. Zhang and Xin [18] significantly improved energy dissipation efficiency by filling the cavity with porous materials. Sun et al. [19] designed a soft-walled space-coiling metamaterial that achieved low-frequency sound absorption through the coupled effects of soft component deformation and channel friction. Bi et al. [20] improved the sound absorption performance of Helmholtz resonators via spatial division and cavity grouping, which simultaneously achieved the dual objectives of enhancing the sound absorption coefficient and realizing broadband sound absorption. Furthermore, the effectiveness of this method in improving sound absorption performance was verified through experiments. Li et al. [21] effectively improved the absorption bandwidth by combining variable-section cavities with perforated plates.

Owing to the excellent sound absorption performance of Helmholtz resonators at their resonant frequencies, researchers have also attempted to combine them with other structures to enhance sound insulation performance. Yamamoto [22] embedded Helmholtz resonator structures into elastic plates and tuned their resonance frequencies to the coincidence frequency of the elastic plate, thereby eliminating the sound insulation valley caused by the coincidence effect. Laly et al. [23] proposed a honeycomb-structured metamaterial composed of 95 neck tubes of varying lengths connected to a porous top plate. This design, Mass law to assemble 95 Helmholtz resonators with different resonance frequencies, achieved a broad sound absorption and insulation frequency band. Langfeldt et al. [24] replaced the mass blocks of conventional metamaterial structures with Helmholtz resonators, which generated an additional sound insulation peak via the Helmholtz resonators. Such multi-mechanism coupling design strategies enable metamaterials to simultaneously possess composite functions like sound insulation, absorption, and vibration isolation, breaking through the performance limitations of single structures.

However, obvious gaps exist in the existing research: although locally resonant metamaterials generate sound insulation peaks within the bandgap, they often form sound insulation valleys outside the bandgap, which severely limits their overall performance; in contrast, Helmholtz resonators are mainly used for sound absorption,

and the research on the coupling mechanism between them and locally resonant structures is insufficient, especially the lack of compensation strategies for sound insulation valleys [25, 26]. This study innovatively proposes a hybrid structure coupling MLRAM with Helmholtz resonators, aiming to address the sound insulation valley problem induced by local resonance. Through impedance analysis and multi-physics field modeling, the valley compensation mechanism is revealed, and the improvement of overall sound insulation performance is experimentally verified. First, the sound insulation performance of MLRAM is systematically investigated. To solve the sound insulation valley problem of MLRAM, a dual-cavity Helmholtz resonator structure is innovatively designed, and the formation mechanism of its sound absorption/sound insulation peaks is revealed via sound pressure level contour maps. MLRAM is optimally integrated with Helmholtz resonators, and a sound, solid thermal multi-physics field coupling model is established. Impedance tube experiments verify the enhanced sound insulation performance of the combined structure. Finally, the effects of geometric parameters and the number of cavities on sound insulation characteristics are explored through parametric studies, and an optimized design scheme is proposed to resolve the sound insulation valley problem.

2. Study on sound insulation characteristics of MLRAM

2.1. Investigation of sound insulation properties of MLRAM

2.1.1. Structural design of MLRAM

To address low-frequency noise control below 400 Hz, an innovative MLRAM structure was designed. As shown in **Figure 1a**, the structure adopts a five-layer configuration: base plate (1 mm)–lower pillars (2 mm)–resonant layer (1 mm)–upper pillars (2 mm)–top plate (1 mm). This embedded resonant structural design overcomes the defect of excessive mass ratio in traditional externally attached resonators, significantly enhancing structural stability through pillar support. **Figure 1b–d** illustrates the geometric features and 4 × 4 periodic arrangement of the structure, with specific parameters listed in **Table 1**. All components are made of aluminum alloy (density 2700 kg/m^3, Young's modulus 70 GPa, Poisson's ratio 0.33, damping coefficient 0.01), ensuring mechanical performance consistency. Different from the conventional externally attached resonators, this embedded design achieves mass ratio optimization and stability enhancement via multi-layer strut support, thereby providing a novel approach for low-frequency control.

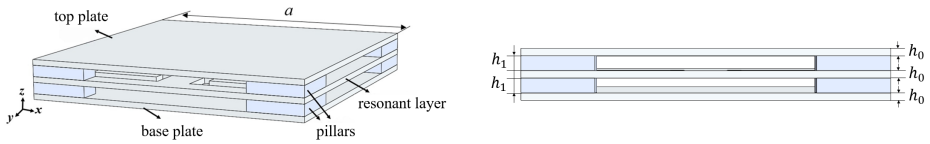

(a) **(b)**

Figure 1. *Cont.*

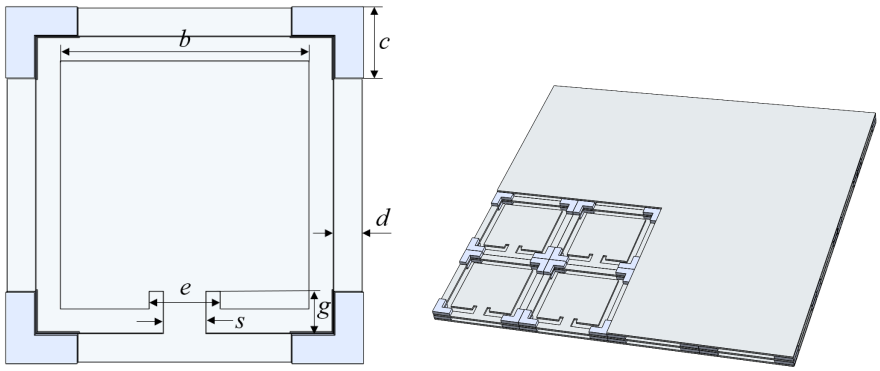

(c) **(d)**

Figure 1. Structural design of MLRAM: **(a)** Unit cell model; **(b)** Side view; **(c)** Top view; **(d)** 4 × 4 periodic arrangement.

Table 1. Geometric parameters of resonant layer.

Parameters	a/(mm)	b/(mm)	c/(mm)	d/(mm)	e/(mm)	s/(mm)	g/(mm)
	50	35	10	4	10	6	6

2.1.2. Analysis of MLRAM sound insulation mechanism

To analyze the bandgap characteristics of MLRAM, band structure calculations were performed using Floquet periodic boundary conditions. Given the periodicity of the structure along the *X*- and *Y*-directions, wave vector parameter scanning was conducted along the *M–Γ–X–M* path (as shown in **Figure 2**) within the first irreducible Brillouin zone. By solving the eigenfrequencies and corresponding vibration modes at different wave vectors, the band structure diagram shown in **Figure 3** was plotted.

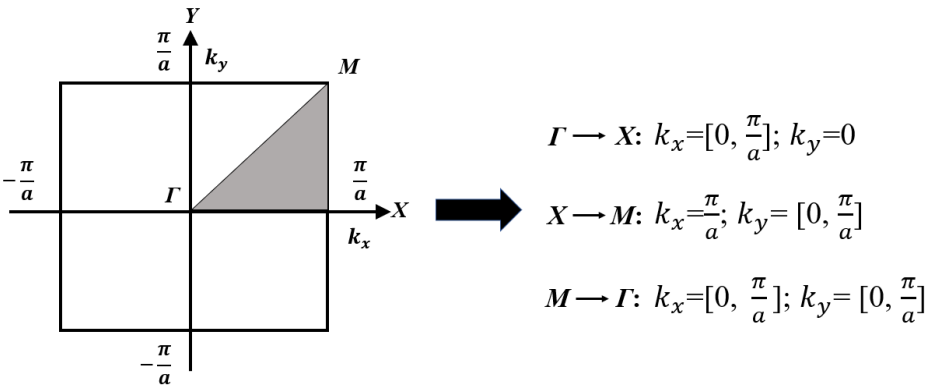

Figure 2. *M–Γ–X–M* path.

Calculation results indicate distinct bandgap features within specific frequency ranges for this MLRAM structure, providing a theoretical basis for its low-frequency vibration control performance. Flat frequency bands in the band structure correspond to local resonance modes, while bandgap formation arises from the synergistic effect of Bragg scattering and local resonance. Analysis of vibration modes at key frequency points (**Figure 4**) reveals that at 179 Hz (Point A), the structure vibrates entirely along the z-axis. Although no bandgap forms, the resonator approaches resonance state, exhibiting a large vibrational displacement. When reaching the bandgap starting point

at 205 Hz (Point B), the resonator generates intense local resonance, concentrating vibrational energy predominantly in the resonant layer while the base plate remains stationary, effectively blocking elastic wave propagation. As frequency increases to 219 Hz (Point C), the local resonance effect diminishes, and the base plate exhibits reverse vibration, leading to bandgap closure. At 294 Hz (Point D), the global vibration pattern indicates the virtual disappearance of local resonance effects.

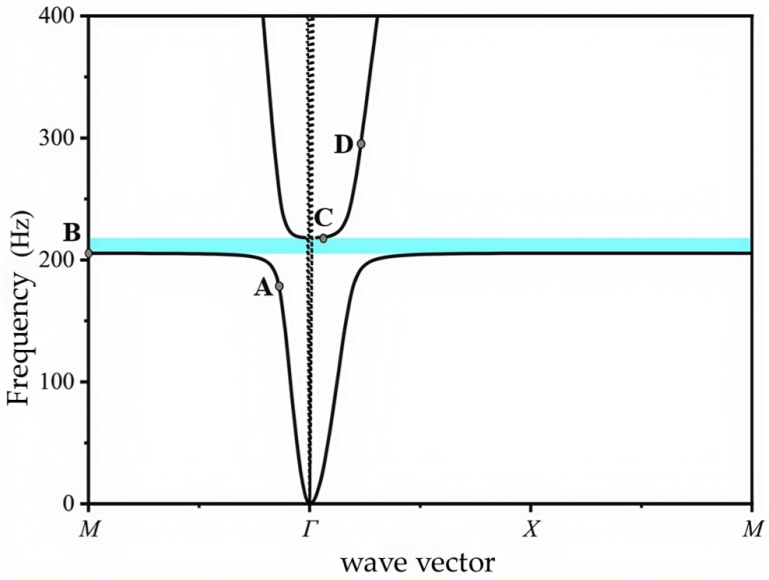

Figure 3. Band structure of MLRAM.

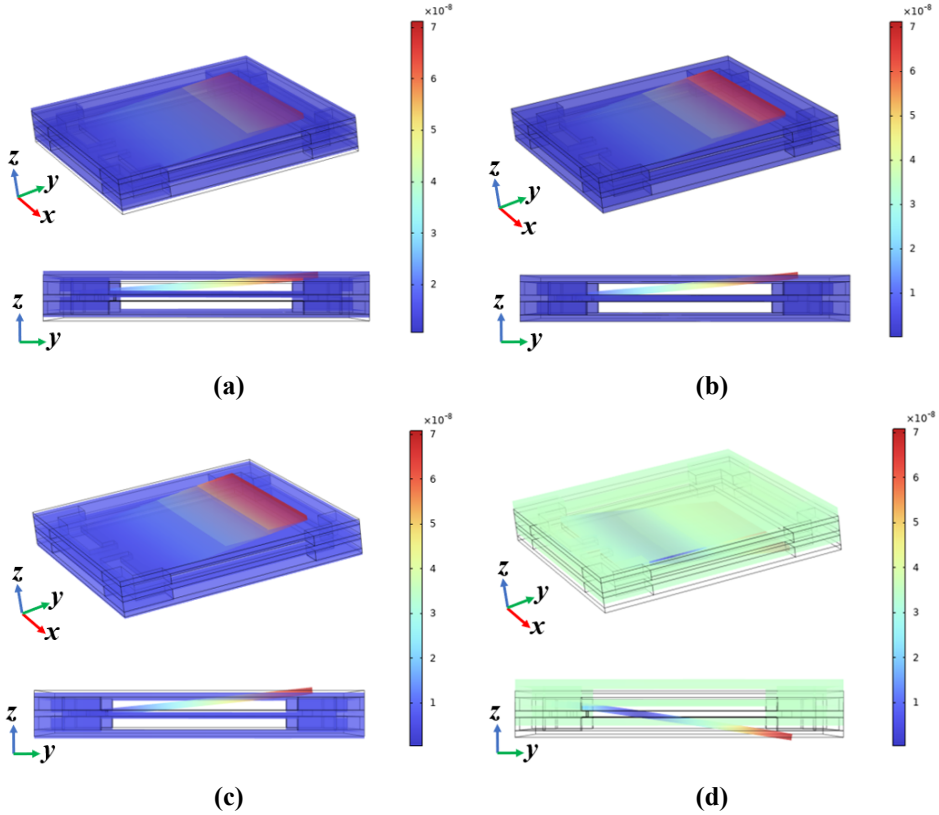

Figure 4. Vibration modes of MLRAM: **(a)** Point A at f = 179 Hz; **(b)** Point B at f = 205 Hz; **(c)** Point C at f = 219 Hz; **(d)** Point D at f = 294 Hz.

2.2. Sound insulation calculation model based on equivalent medium theory

Assuming $p_{1\mathrm{r}}$ represents a harmonic plane wave incident obliquely on the surface of the metamaterial plate, as shown in **Figure 5**, p_{ref} and p_{tr} denote the reflected and transmitted sound waves generated by the incident wave, respectively. The wave vector of the sound wave is denoted by k_0, with θ and φ representing its elevation and azimuth angles. Decomposed in the Cartesian coordinate system, it is expressed as:

$$k_0 = (k_x, k_y, k_z) \tag{1}$$

where

$$k_x = k_0 \sin\theta \cos\varphi, k_y = k_0 \sin\theta \sin\varphi, k_z = k_0 \cos\theta,\ k_0 = \frac{\omega}{c_0} \tag{2}$$

Here, ω is the angular frequency and c_0 is the speed of sound. The incident sound wave p_{in} can be expressed as:

$$p_{\mathrm{mc}}(x, y, z, t) = p_{\mathrm{mc}}(x, y, z)e^{\mathrm{i}\alpha t} = p_0 e^{-\mathrm{i}(k_x + k_y + k_z)x} e^{\mathrm{i}\alpha t} \tag{3}$$

where P_{i0} denotes the incident wave amplitude. Let $\mathrm{r} = (x, y)$ and $\mathrm{k} = (k_x, k_y)$, then:

$$p_{\mathrm{in}}(\mathrm{r}, Z) = p_{10}\varepsilon^{-\mathrm{k}\cdot\mathrm{r}}\varepsilon^{-k_z} \tag{4}$$

Similarly

$$p_{ref}(\mathrm{r}, z) = p_{00}e^{-\mathrm{k}\cdot\mathrm{r}}e^{\mathrm{k}\cdot z}, p_{\mathrm{tr}}(\mathrm{r}, z) = p_{00}e^{-\mathrm{k}\cdot\mathrm{r}}e^{-\mathrm{k}\cdot z} \tag{5}$$

where p_0 and p_{t0} correspond to the reflected and transmitted wave amplitudes, respectively.

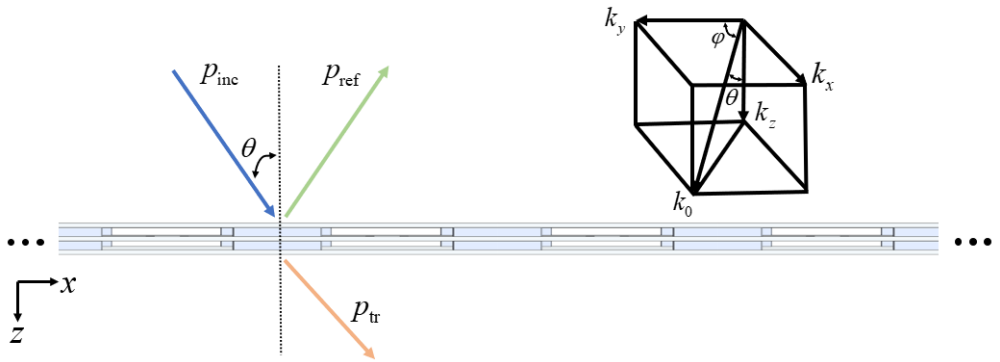

Figure 5. Schematic diagram of sound wave incident on metamaterial surface.

This study establishes a theoretical sound insulation calculation model for MLRAM based on Equivalent Medium Theory [18]. In the 10–400 Hz frequency range, the ratio of unit cell size to the minimum wavelength ($\lambda/a \approx 0.058$) satisfies the long-wave assumption, allowing the metamaterial to be equivalently treated as a homogeneous plate with dynamic mass density. As illustrated in **Figure 6**, the resonator in MLRAM's resonant layer can be simplified as a concentrated mass block, the elastic beams as springs, and the remaining components as the base plate.

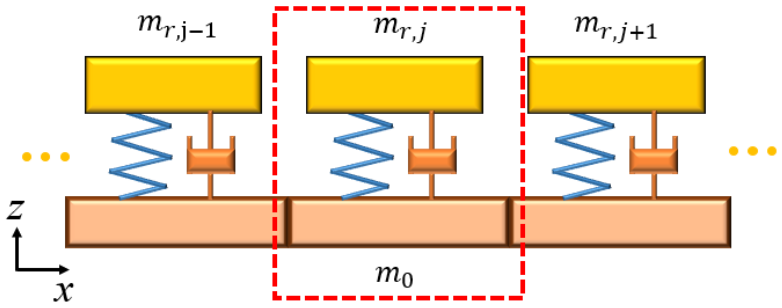

Figure 6. Simplified model of metamaterial structure.

In the equivalent model, the equivalent dynamic mass of the resonator structure is:

$$m_{equiv,j} = \frac{m_{r,j}}{1 - \omega^2 \left[\omega_j^2 (1 + \eta_{r,j})\right]} \tag{6}$$

where m_r is the resonator mass, $\omega = 2\pi f, f$ is the angular frequency of the incident wave, ω_γ is the resonant angular frequency of the local resonator, and η is the damping coefficient.

The equivalent masses of all resonators in a single unit cell are superimposed and homogenized into the mass component of the base plate. The equivalent dynamic mass density of the metamaterial plate is calculated as:

$$\rho_{eff}(\omega) = \left(\rho Sh + \sum_{j=1}^{N} m_{equiv,j}\right) \frac{1}{Sh} = \rho + \sum_{j=1}^{N} \frac{\rho_j}{1 - \omega^2 / \left[\omega_j^2 (1 + i\eta_j)\right]} \tag{7}$$

where

$$\rho_j = m_j / Sh \tag{8}$$

Here, ρ is the density of the base plate; S represents the surface area of the base plate within a single unit cell; h is the thickness of the base plate. From the above, the equivalent dynamic mass surface density of the metamaterial structure can be calculated as:

$$\rho_s = (\rho Sh + \sum_{j=1}^{N} m_{equiv,j}) \frac{1}{a^2} \tag{9}$$

where a is the metamaterial unit cell size. The mass ratio between the resonators and the base plate in the metamaterial plate is:

$$\gamma = \sum_{j=1}^{N} m_j / \rho Sh = \sum_{j=1}^{N} \rho_j / \rho \tag{10}$$

The bending wave number of the metamaterial plate can be obtained from the equivalent dynamic density ρ_{eff}:

$$k_{p,\text{eff}}^4 = \rho_{\text{eff}} h \omega^2 / D \tag{11}$$

where $D = Eh^3/12(1-v^2)$ represents the bending stiffness of the plate; E and v denote the Young's modulus and Poisson's ratio of the base plate material. Under acoustic

excitation, the equation of motion for the metamaterial plate is expressed as:

$$D\nabla^4 w(\mathrm{r}) - \rho_{eff} h\omega^2 w(r) = p_{\mathrm{inc}}(\mathrm{r}, z)_{z=0} + p_{\mathrm{ref}}(\mathrm{r}, z)_{z=0} - p_{\mathrm{rr}}(\mathrm{r}, Z)_{z=0} \tag{12}$$

where $\nabla^4 = \left(\partial^2/\partial x^2 + \partial^2/\partial y^2\right)^2$ represents the transverse vibration displacement of the metamaterial plate.

Since the incident sound wave is a harmonic plane wave, the vibration displacement of the metamaterial plate, as well as the solutions for reflected and transmitted sound waves, can be assumed to be in plane wave form. The sound power transmission coefficient under oblique incidence can be obtained by combining the continuity conditions of acoustic-solid coupling:

$$\tau_p(\theta, \varphi) = \tau_p(\theta) = \left| \frac{2\rho_0 c_0 \omega}{\Delta(\omega)\cos\theta} \right|^2 \tag{13}$$

where

$$\Delta(\omega) = D(k_0 \sin\theta)^4 - \rho_{eff} h\omega^2 + 2i\rho_0 c_0 \omega / \cos\theta \tag{14}$$

Furthermore, the sound power transmission coefficient in a diffuse sound field is:

$$\tau_{\mathrm{diff}} = \frac{\int_0^{\pi/2} \tau_p(\theta) \sin\theta \cos\theta \mathrm{d}\theta}{\int_0^{\pi/2} \sin\theta \cos\theta \mathrm{d}\theta} = \int_0^{\pi/2} \tau_p(\theta) \sin 2\theta \mathrm{d}\theta \tag{15}$$

The sound transmission loss for oblique incidence (τ_p) or diffuse sound field (τ_{diff}) is:

$$STL = 10 \lg\left(\frac{1}{\tau}\right) \tag{16}$$

For the MLRAM designed in this study, the resonator mass m_r is 0.003 kg, its resonance frequency f_r is 205 Hz, damping coefficient η is 0.01, and the remaining structure is simplified as a thin aluminum plate. The plate side length a is 50 mm, mass m_0 is 0.0183 kg, height h is 0.0027 m. The calculated sound insulation characteristic curve is shown in **Figure 7**.

The sound insulation characteristic curve in **Figure 7** reveals the unique acoustic performance of MLRAM: in the low-frequency region (<200 Hz), it follows the conventional mass law, with sound insulation increasing linearly with frequency; whereas within the 205–218 Hz bandgap range, the structure breaks the mass law limitation, generating a significant sound insulation peak of 45.9 dB at 214 Hz, which is 22.6 dB higher than that of a homogeneous plate with equivalent mass. This anomalous sound insulation enhancement originates from the wave impedance mismatch induced by local resonance. However, the 5.6 dB sound insulation valley at 231 Hz (18.3 dB lower than the homogeneous plate) indicates that while local resonance suppresses sound propagation in specific frequency bands, it enhances sound transmission in adjacent frequency bands.

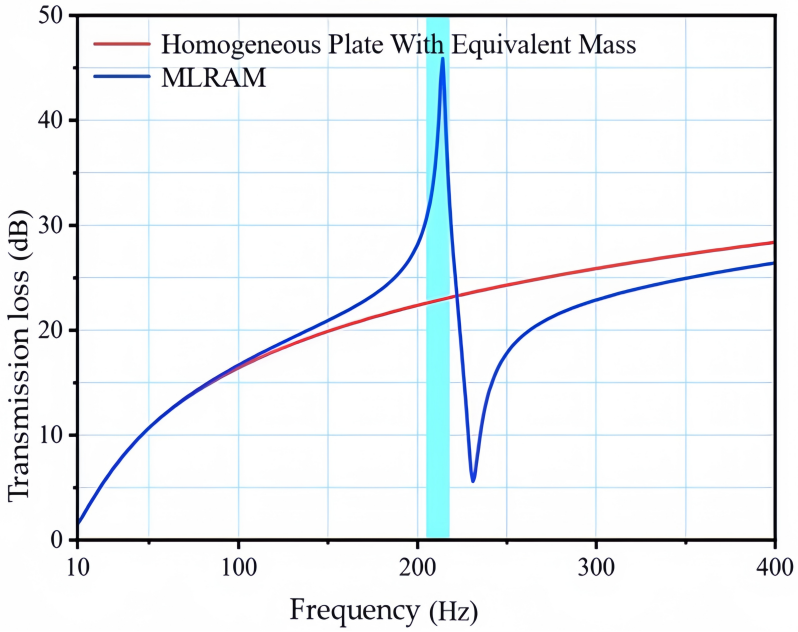

Figure 7. Sound insulation characteristic curve of the MLRAM.

2.3. Sound insulation characteristic calculation

This study employs a fluid-solid coupling numerical method to investigate the sound insulation characteristics of MLRAM, utilizing the Solid Mechanics-Pressure Acoustics multiphysics coupling module in COMSOL software for simulation. As shown in **Figure 8**, the FEM results indicate that MLRAM exhibits a significant sound insulation peak of 44.5 dB at 214 Hz—substantially higher than that of an equivalent-mass homogeneous plate—while a sound insulation valley of 6.4 dB occurs at 228 Hz. Subsequent analyses are based entirely on FEM calculation results.

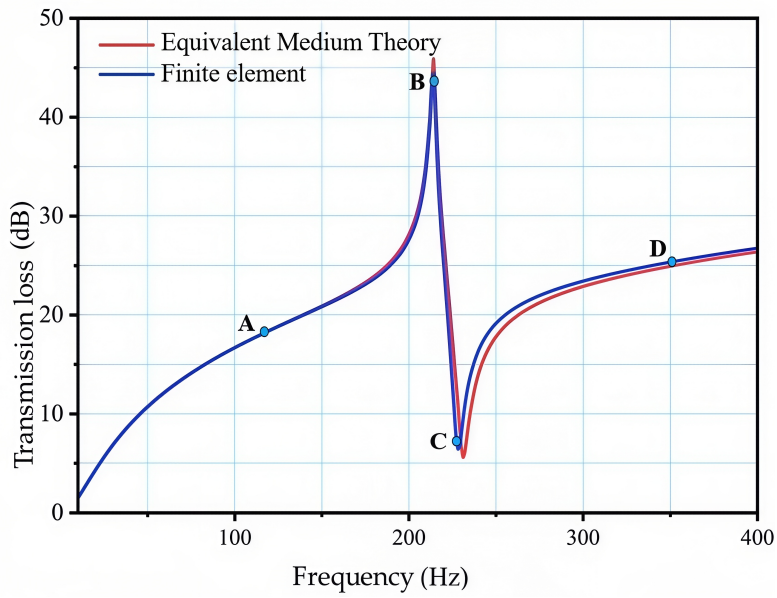

Figure 8. Comparison of calculated results for MLRAM sound insulation curves.

3. Study on sound insulation characteristics of metamaterial composite structures

Previous research investigated the sound insulation properties of MLRAM, which exhibit a sound insulation peak significantly higher than that of an equivalent-mass homogeneous panel within the band gap frequency range. However, this is followed by a sound insulation valley in frequencies outside the band gap. To address this issue, this chapter proposes a composite structure combining locally resonant metamaterials with Helmholtz resonators. Helmholtz resonators generate both an absorption peak and a sound insulation peak at their resonant frequency. By leveraging this characteristic, the composite structure enhances the sound insulation performance of MLRAM in frequency bands with weak insulation, thereby improving its overall sound insulation capability.

3.1. Study on acoustic characteristics of Helmholtz resonators

Helmholtz resonator-type metamaterials generate significant absorption peaks at resonant frequencies through cavity air resonance and neck viscous dissipation. Studies indicate that this structure also forms a sound insulation peak on the sound insulation curve. By adjusting geometric parameters, its resonant frequency can be tuned to match target frequency bands for sound insulation applications. To address the sound insulation valley issue in MLRAM, a dual-cavity Helmholtz resonator structure is designed (**Figure 9**). This structure consists of two equally sized perforated cavities with necks of different apertures. Specific parameters are: length and width 50 mm, height 24 mm, neck length 21 mm, aperture diameters 2.0 mm and 2.7 mm, and wall thickness 0.6 mm. Manufactured from ABS resin, its mass matches that of the MLRAM top plate. This dual-cavity design innovatively achieves dual resonance peaks via different neck apertures, directly compensating for the sound insulation valley problem of MLRAM, which distinguishes it from the conventional single-cavity design.

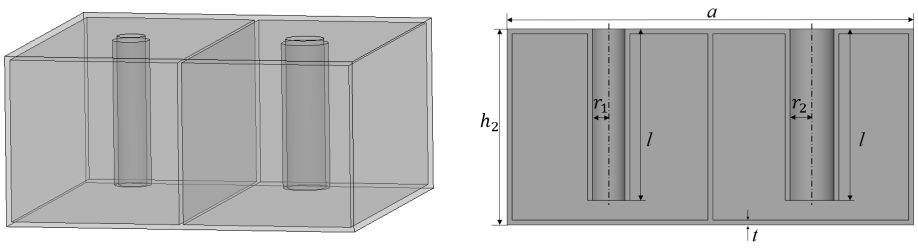

(a) **(b)**

Figure 9. Dual-cavity Helmholtz resonator model and geometric parameters: **(a)** Geometric structure; **(b)** Geometric parameters.

The thickness of the thermoviscous boundary layer can be calculated as:

$$d_V = \sqrt{\frac{\mu}{\pi \rho_0 f_{\max}}} \tag{17}$$

In the equation, $\mu = 1.814 \times 10^{-5}$ Pa·s represents the dynamic viscosity of air. When the maximum solving frequency is 400 Hz, substituting into Equation (17) yields

a thermoviscous boundary layer mesh thickness of 0.11 mm.

All other domains in the model are configured as pressure acoustics, with hard sound field boundary conditions applied to all boundaries except the perfectly matched layer. Swept meshing is used for the perfectly matched layer and the air domain at the neck, while free tetrahedral meshing is adopted for other regions. To ensure computational accuracy, the maximum mesh size is set to $c_0/6f_{\max}$ and the minimum size to $c_0/10f_{\max}$, where $f_{\max}$ is the maximum solving frequency. By performing domain integration over the incident air domain, the sound intensity reflection coefficient r and absorption coefficient α of the Helmholtz resonator structure are obtained:

$$r = \int \frac{p_s^2}{p_b^2} dV \tag{18}$$

$$\alpha = 1 - |r|^2 \tag{19}$$

where V is the volume of the incident air domain, p_s denotes the scattered sound pressure in the incident domain, and p_b represents the total background sound pressure in the incident air domain.

The sound absorption characteristic curve of the dual-cavity Helmholtz resonator structure (**Figure 10**) exhibits a dual-peak feature: absorption peaks occur at 236 Hz and 316 Hz, both with peak absorption coefficients reaching 0.99, achieving near-perfect sound absorption. Between these peaks, an absorption trough (α = 0.21) exists at 282 Hz. The overall trend demonstrates that the sound absorption coefficient increases with frequency in the low-frequency range until reaching the first peak, subsequently decreases to the trough, then rises to the second peak, and finally gradually decays as frequency increases. This structure demonstrates excellent broadband sound absorption performance within the target frequency range (200–350 Hz).

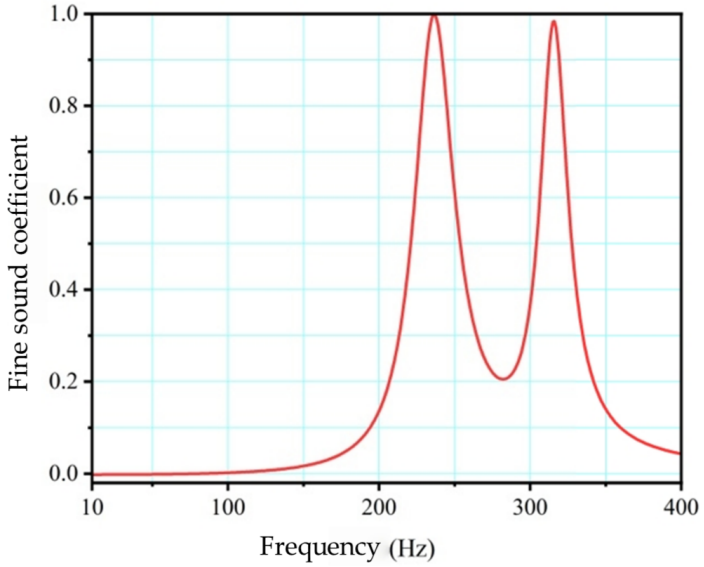

Figure 10. Sound absorption characteristic curve of the dual-cavity Helmholtz resonator structure.

Good sound absorption performance requires proper impedance matching; that is, the real part (acoustic resistance) of the structural surface impedance ratio reaches

1 and the imaginary part (acoustic reactance) approaches zero. This indicates that the structural impedance is perfectly matched with the air impedance, thus achieving perfect sound absorption of acoustic waves. The calculated normalized acoustic impedance curves of the dual-cavity Helmholtz resonator structure are illustrated in the **Figure 11** below. A comparison of the two sound absorption peaks and the sound absorption trough shows that the higher the sound absorption coefficient, the closer the normalized acoustic resistance x_s of the structure is to 1, which means a better matching degree between the structural impedance and the air impedance and thus a superior sound absorption effect. A sound absorption trough appears between the two sound absorption peaks; at this point, the lower the sound absorption coefficient, the larger the normalized acoustic resistance x_s, which deviates further from 1. This implies that the matching degree between the structural impedance and the air impedance decreases, leading to a weakened sound absorption effect. At the frequency corresponding to each sound absorption peak, the normalized acoustic reactance y_s of the structure crosses zero at this moment, the structure resonates and dissipates acoustic wave energy, consequently generating the sound absorption peak.

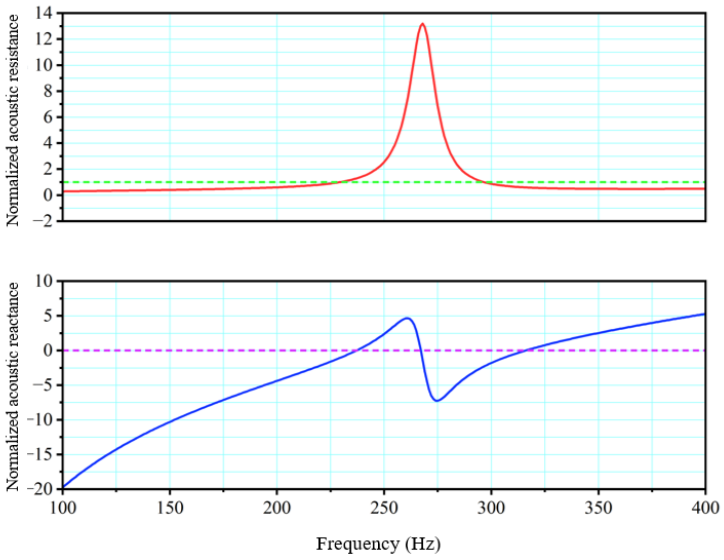

Figure 11. Normalized acoustic impedance curves of the dual-cavity Helmholtz resonator structure.

The sound insulation characteristic curve of the dual-cavity Helmholtz resonator structure is presented in **Figure 12**, revealing typical resonance-controlled features. The absorption curve (solid red line) represents the sound absorption coefficient of the structure. It reflects the proportion of incident sound wave energy that is consumed by the structure (mainly converted into heat energy). Sound Insulation Curve (black dashed line): This curve represents the sound transmission loss of a structure. It measures the structure's ability to block sound wave propagation, which is the logarithmic value of the ratio between incident sound energy and transmitted sound energy. The higher the STL value, the better the sound insulation performance. Sound insulation peaks of 18.3 dB and 24.4 dB occur at 232 Hz and 311 Hz, respectively, exceeding the mass law predictions by 4.4 dB and 8.0 dB. The low-frequency sound insulation performance follows the mass law, while near the

cavity resonance frequencies, the sound insulation loss exhibits a significant leap, forming peaks before returning to the mass law growth trend. This phenomenon confirms that while generating absorption peaks, the Helmholtz resonator structure simultaneously produces significant sound insulation enhancement effects within the same frequency bands. The two sound insulation peaks correspond to the two resonance peaks (236 Hz and 316 Hz) in the absorption curve, verifying the frequency-domain consistency between sound absorption and insulation performance.

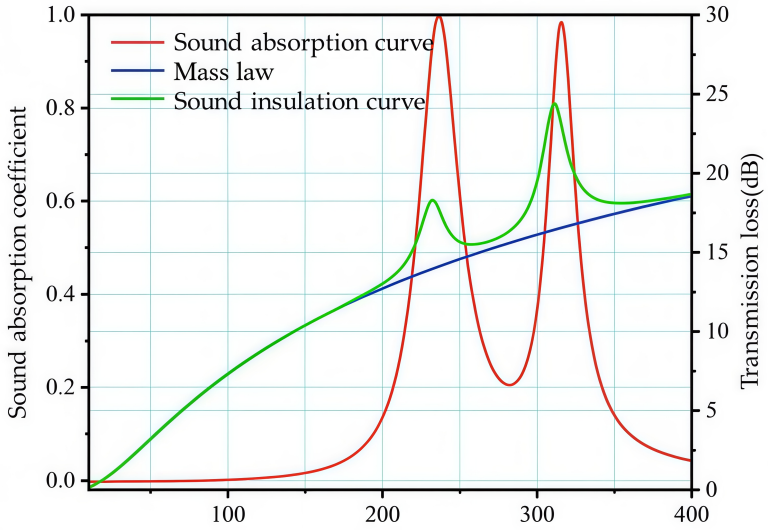

Figure 12. Sound absorption coefficient, sound insulation loss, and mass law reference of the Helmholtz resonator structure.

The displacement deformation contour maps of the dual-cavity Helmholtz resonator structure at its two resonant frequencies are illustrated in **Figure 13**. As can be seen from **Figure 13**, the left cavity corresponds to the first resonant frequency. At this frequency, the air inside the neck of the left cavity resonates, which in turn drives the vibration and displacement of the neck. This dissipates the incident acoustic energy, yielding excellent sound absorption and insulation performance, and thus generating a sound absorption peak and a sound insulation peak at this frequency. Similarly, the right cavity corresponds to the second resonant frequency. At this frequency, the air inside the neck of the right cavity resonates, causing the vibration and displacement of the neck. The incident acoustic energy is then dissipated, consequently producing a second sound absorption peak and a second sound insulation peak.

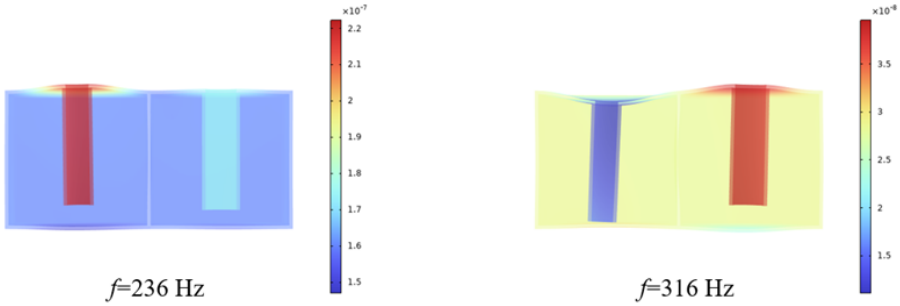

Figure 13. Displacement contour maps of the dual-cavity Helmholtz resonator structure at resonant frequencies.

3.2. Calculation of sound insulation characteristics for metamaterial composite structure

Although MLRAM generates significant sound insulation peaks within the bandgap, its inherent peak-valley characteristic (i.e., the emergence of sound insulation valleys outside the bandgap) limits the overall performance. To achieve broadband low-frequency sound insulation, it is imperative to address this sound insulation valley problem. This study innovatively proposes a coupling strategy: leveraging the characteristic of Helmholtz resonators that generate both sound absorption peaks and sound insulation peaks at their resonant frequencies [16], the resonators are integrated with MLRAM. The core physical principle is as follows: by precisely designing the resonant frequencies of the Helmholtz resonators, their sound insulation peaks are aligned with the sound insulation valleys of MLRAM, thereby yielding a trough compensation effect. Accordingly, a novel metamaterial composite structure is constructed by combining the dual-cavity Helmholtz resonator structure with MLRAM (**Figure 14**). This structure replaces the original top plate with a dual-cavity Helmholtz resonator. This design not only preserves the original mass but also achieves synergistic enhancement of sound insulation performance through the superposition of acoustic functions.

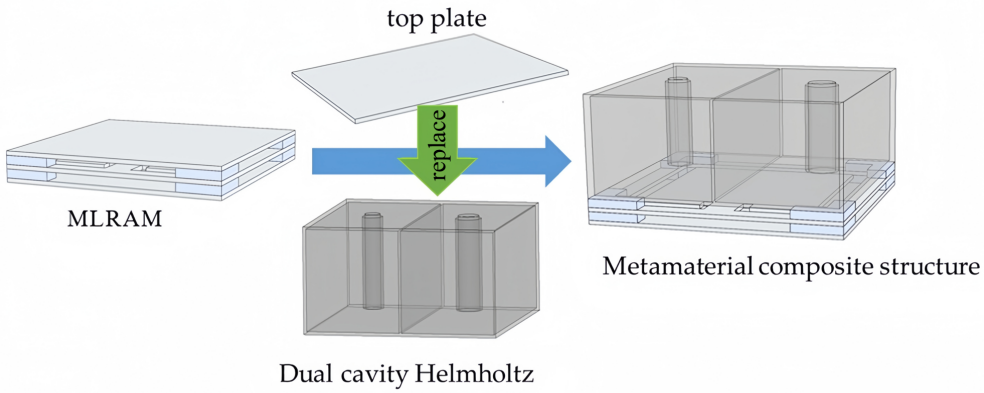

Figure 14. Design of the metamaterial composite structure.

A sound insulation calculation model of the composite structure was established in this study. The Floquet periodic boundary conditions were applied to the incident/transmitted air domains and structural boundaries in the model to simulate the infinitely periodic structure. A sound-solid-thermal multi-physics coupling method was adopted to accurately capture the variations in acoustic characteristics of different regions (e.g., resonator necks, cavities, and substrate structures).

A comparison of sound insulation curves between the composite structure and MLRAM is shown in **Figure 15**. The sound insulation curve of the composite structure exhibits a "peak-valley-peak (P1-V-P2)" characteristic. The composite structure exhibits improved sound insulation performance in the trough and subsequent frequency bands compared to the original structure. At the 228 Hz trough, the composite achieves 9.4 dB of sound insulation loss, representing a 3.0 dB enhancement over the original structure. A second sound insulation peak emerges at 311 Hz with a value of 32.0 dB, marking an 8.1 dB improvement. The sound insulation performance

of the uniform quality board (red line) in the **Figure 15** should theoretically comply with the Mass law.

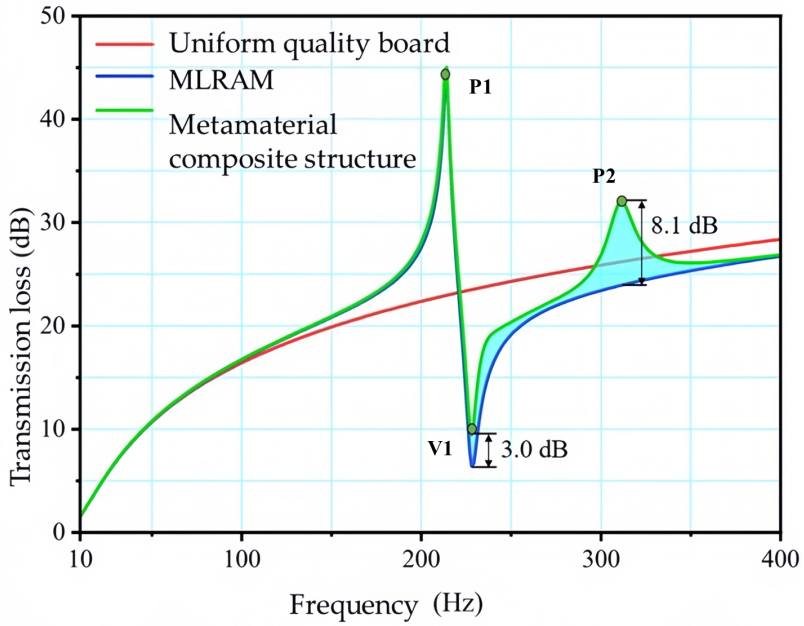

Figure 15. Comparison of sound insulation characteristic curves for the metamaterial composite structure.

Within the 10–400 Hz frequency range, the average sound insulation losses for the homogeneous plate, MLRAM, and composite structure are 20.7 dB, 20.0 dB, and 21.0 dB, respectively. Although MLRAM exhibits significant insulation peaks in specific bands, its overall performance slightly lags behind the homogeneous plate due to insulation troughs. In contrast, by incorporating Helmholtz resonators, the composite structure effectively mitigates insulation troughs and generates a second insulation peak while maintaining constant mass, ultimately achieving superior overall sound insulation performance compared to the homogeneous plate. **Figure 16** illustrates the sound pressure level cloud distribution characteristics of the composite structure at key frequencies. The enhanced performance of the composite structure in the sound insulation valley and subsequent frequency bands stems from the resonant dissipation mechanism introduced by the Helmholtz resonators. As illustrated in **Figure 16**, at the sound insulation valley frequency (228 Hz, Point C), the left cavity resonates, and acoustic energy is highly concentrated in its neck region (see the acoustic energy density contour maps in **Figure 17**). Acoustic wave energy is converted into thermal energy and dissipated via the thermoviscous effect, thereby effectively filling the inherent sound insulation valley of MLRAM. In contrast, the second sound insulation peak appearing at 311 Hz (Point D) is dominated by the resonance of the right cavity. This validates the conclusion presented in Section 3.1: the sound absorption peaks of Helmholtz resonators correspond to sound insulation peaks, and their coupling effect achieves active compensation for the acoustic defects of MLRAM.

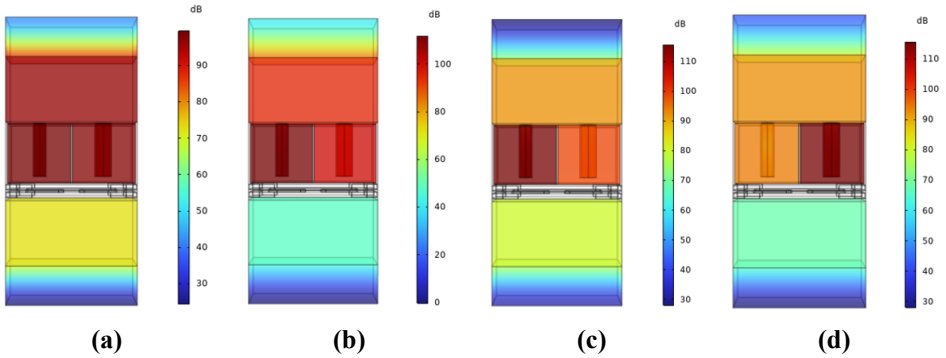

Figure 16. Sound pressure level cloud distributions of the metamaterial composite structure: **(a)** Point A at f = 115 Hz; **(b)** Point B at f = 214 Hz; **(c)** Point C at f = 228 Hz; **(d)** Point D at f = 311 Hz.

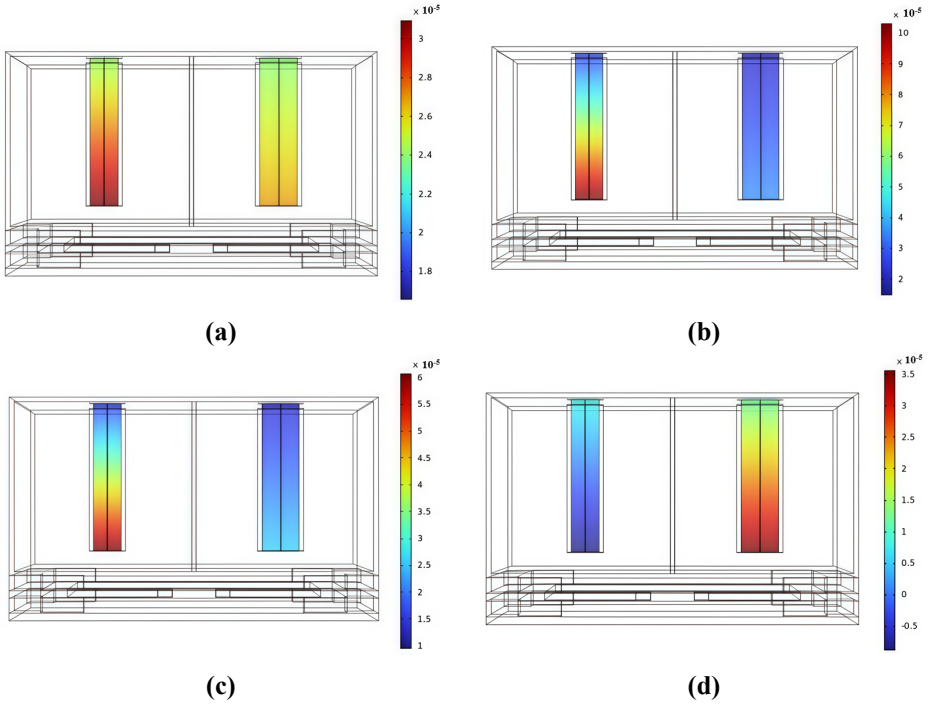

Figure 17. Sound energy density distribution clouds of the metamaterial composite structure: **(a)** Point A at f = 115 Hz; **(b)** Point B at f = 214 Hz; **(c)** Point C at f = 228 Hz; **(d)** Point D at f = 311 Hz.

As shown in **Figure 17**, the metamaterial composite structure exhibits distinct sound pressure distribution characteristics at different feature frequencies. At 115 Hz (Point A), both cavities of the Helmholtz resonator show high sound pressure without reaching resonance, and sound insulation primarily follows the mass law. At 214 Hz (Point B), the bottom MLRAM generates the first sound insulation peak (44.5 dB) with significantly reduced sound pressure, while the left cavity approaches its resonance frequency. The sound insulation valley at 228 Hz (Point C, 6.4 dB) is notably improved through resonant dissipation in the left cavity. At 311 Hz (Point D), the right cavity dominates to produce the second sound insulation peak (24.4 dB). Research confirms that the absorption peaks of the Helmholtz resonator correspond to sound insulation peaks. Its first resonance peak effectively compensates for MLRAM's insulation trough, while the secondary peak extends the structure's insulation bandwidth. Their

synergistic interaction achieves broadband sound insulation enhancement.

Sound energy density characterizes the total vibrational energy per unit volume (J/m^3), comprising kinetic energy density (particle vibration) and potential energy density (medium deformation). **Figure 17** presents cloud distributions of sound energy density in the neck tube regions of both cavities at key frequencies, visually reflecting spatial energy distribution characteristics.

Figure 17 reveals that at 115 Hz (Point A), sound energy distributes uniformly across both neck tubes and increases with depth, indicating non-resonant states in both cavities. At 214 Hz (Point B), the left neck tube exhibits significantly higher energy density than the right, suggesting proximity to the left cavity's resonance frequency. At 228 Hz (Point C), resonance in the left cavity concentrates acoustic energy intensely within its neck tube, effectively mitigating the composite structure's insulation trough. At 311 Hz (Point D), resonance in the right cavity shifts energy concentration to its neck tube, forming the second insulation peak and enhancing overall performance.

3.3. Sound insulation test analysis

This section validates the accuracy of finite element simulations and the effectiveness of Helmholtz resonators in enhancing MLRAM sound insulation through impedance tube experiments. The composite structure specimen was tested using a B&K acoustic impedance tube system (Type 7758), comprising an impedance tube, PULSE software platform, data acquisition unit, signal generator, and power amplifier, as shown in **Figure 18**. The testing principle involves generating a plane wave excitation along the normal direction, with two sets of acoustic sensors in the front and rear tubes acquiring sound pressure values to calculate transfer functions. The transmission coefficient and sound insulation loss are then derived using the transfer matrix method.

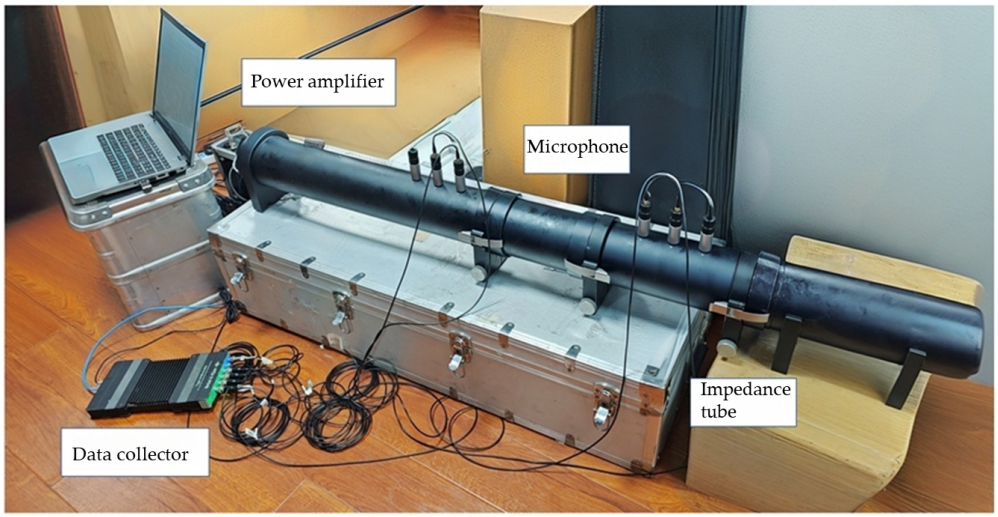

Figure 18. Impedance tube experimental setup.

To meet impedance tube requirements, a 3D-printed unit cell structure was fabricated as the test specimen (**Figure 19**). For low-to-mid frequency testing, a standard large tube with a 100 mm diameter was used, paired with a resin base of identical dimensions. The specimen consists of three components: **Figure 19a**

illustrates the overall structure; **Figure 19b** shows the aluminum alloy MLRAM substructure; **Figure 19c** displays the resin Helmholtz resonator; **Figure 19d** presents the assembled composite structure. All components were precision-manufactured via 3D printing to ensure consistency with simulation models.

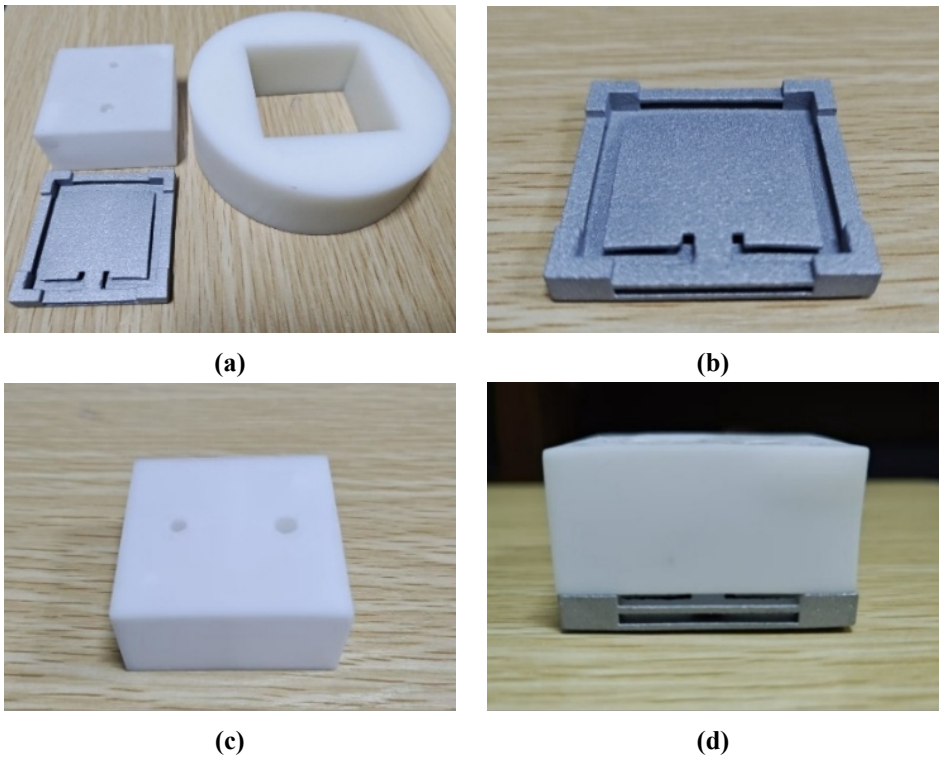

(a) **(b)**

(c) **(d)**

Figure 19. 3D-printed metamaterial samples for testing: **(a)** Metamaterial with base; **(b)** MLRAM structure; **(c)** Helmholtz resonator structure; **(d)** Composite metamaterial structure.

The test samples of the metamaterial composite structure were embedded in the base, which were then mounted in the impedance tube. To avoid gaps between the samples and the base as well as between the base and the impedance tube, petroleum jelly was applied at these interfaces. After completing the sample installation and impedance tube connection, relevant parameters were set in the test software to conduct the measurements. Since the sound insulation curves obtained in the experiments were those of a single cell of the metamaterial composite structure, the results derived from the comparative simulation calculations were also required to be the sound insulation characteristic curves of a single cell. In the simulations, the boundary conditions around the composite structure were set as prescribed displacements, where the prescribed displacements in the x and y directions were zero while the z direction was free. With other settings kept unchanged, the sound insulation characteristic curves were calculated accordingly.

The sound insulation curve of the unit cell structure in **Figure 20** exhibits low-frequency shifts in peak/trough positions compared to infinite periodic structures, attributable to boundary-condition-induced resonance frequency changes in the underlying substructure. Both experimental and simulated curves display identical "peak-trough-peak" characteristic sequences, confirming the multiphysics model's reliability.

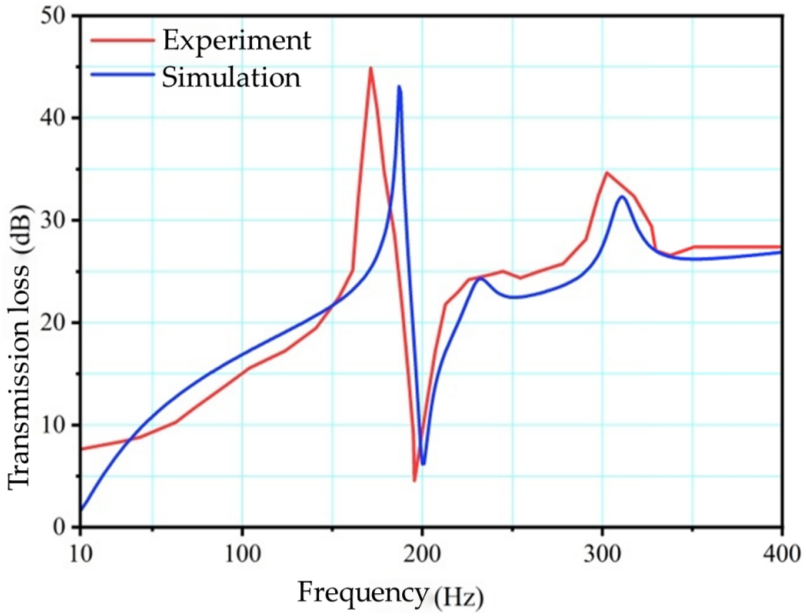

Figure 20. Comparison of experimental and simulated results.

Discrepancies between measurements and simulations include: the first insulation peak occurs at 171 Hz (experiment) versus 187 Hz (simulation), with generally higher experimental insulation loss in subsequent bands. These deviations primarily arise from: (1) Manufacturing tolerances, particularly dimensional variations in 0.6 mm-thick Helmholtz resonator walls during 3D printing; (2) Material property differences between actual aluminum alloy/resin and simulation models; (3) Boundary condition variations, including assembly gaps preventing ideal experimental replication of simulated constraints. Collectively, these factors impact measurement precision.

3.4. Analysis of key influencing factors

3.4.1. Geometric parameters

As shown in **Figure 21**, compared with the original composite structure, a decrease in r_1 shifts the "compensation effect" induced by the Helmholtz resonator toward lower frequencies, which increases the sound insulation loss at the first peak while reducing the sound insulation loss at the trough to the same level as that of the original locally resonant structure. An increase in r_1 shifts the compensation effect toward higher frequencies, which is characterized by the emergence of a new sound insulation peak in the frequency band after the trough. In addition, a gradual increase in r_2 from 2.5 mm to 2.9 mm leads to a gradual shift of the sound insulation peak generated by the Helmholtz resonator toward higher frequencies.

With the aperture size kept constant, the neck lengths of the Helmholtz resonator structure were set to 19 mm, 20 mm, 21 mm, and 22 mm, respectively. The calculated sound insulation characteristic curves of the metamaterial composite structure are shown in **Figure 22**.

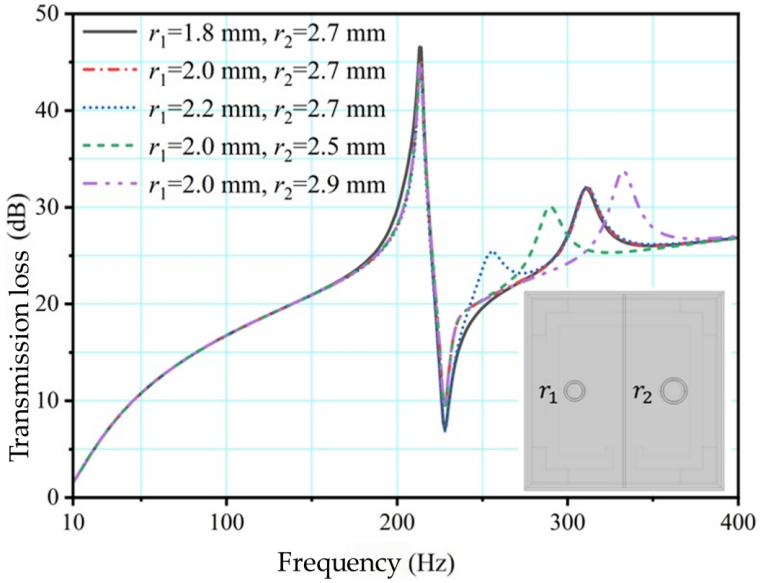

Figure 21. Influence of aperture size on sound insulation performance.

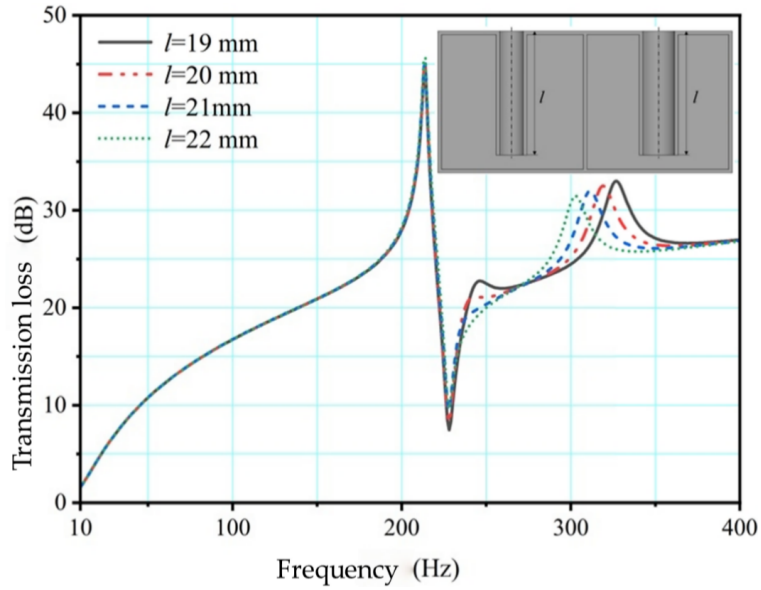

Figure 22. Influence of neck tube length l on sound insulation performance.

For the left cavity, as its parameter gradually increases, the "compensation effect" induced by it shifts toward lower frequencies gradually, which is manifested by the emergence of a sound insulation peak in the frequency band after the trough, an increase in sound insulation loss at the trough, and an enhancement in sound insulation loss at the first peak, respectively. For the right cavity, as its parameter increases gradually, the second sound insulation peak generated by it shifts toward lower frequencies gradually. When the aperture size decreases or the neck length increases, the sound absorption peak of the Helmholtz resonator structure shifts toward lower frequencies, and the sound insulation peak on the sound insulation curve also shifts toward lower frequencies; similarly, when the aperture size increases or the neck length decreases, the sound insulation peak shifts toward higher frequencies. By adjusting the structural parameters, the sound absorption peak of the Helmholtz resonator structure can be tuned to the sound insulation valley or weak regions, thereby improving the overall sound

insulation performance of the structure.

3.4.2. Cavity quantity

On the basis of the dual-cavity Helmholtz resonator composite structure, composite structures with three and four perforated cavities were designed separately, as illustrated in **Figure 23**. Specifically, the aperture sizes of the three-cavity composite structure were set as r_1 = 2.0 mm, r_2 = 1.8 mm and r_3 = 2.0 mm; while those of the four-cavity composite structure were set as r_1 = 1.4 mm, r_2 = 1.6 mm, r_3 = 1.8 mm and r_4 = 2.0 mm. To maintain the same mass as the original composite structure, the wall thicknesses of the two structures were set to 0.55 mm and 0.52 mm, respectively, with all other geometric parameters kept.

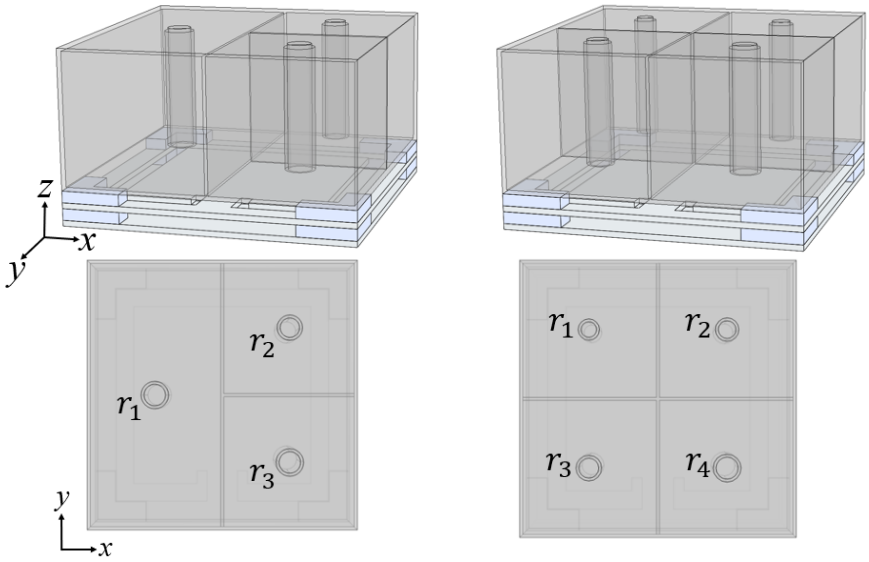

Figure 23. Metamaterial composite structures with varying cavity quantities: **(a)** Triple-cavity; **(b)** Quadruple-cavity.

The calculated sound insulation characteristic curves of the two structures are shown in **Figure 24**. Both the dual-cavity composite structure and the three-cavity composite structure exhibit a higher STL of 9.4 dB at the sound insulation valley compared with other structures. The difference lies in that the former generates only one new sound insulation peak in the subsequent frequency band, while the latter generates two peaks in the same frequency range, with the peak value of the former being much higher than that of the latter. In comparison with the three-cavity composite structure, the four-cavity composite structure produces an additional sound insulation peak in the subsequent frequency band, but its STL at the sound insulation valley is lower than that of the three-cavity structure.

Compared with the dual-cavity composite structure, the three-cavity composite structure has an increased number of cavities and a reduced volume of the single right cavity, which results in an unchanged STL at the trough, an expanded range of STL improvement in the sound insulation weak frequency bands, and a decreased improvement amplitude. Similarly, the four-cavity composite structure also has an increased number of cavities, with the volumes of both the left and right cavities

reduced; this leads to a decreased STL improvement at the trough and a further expanded range of STL improvement in the weak frequency bands. A comparison of the sound insulation peaks generated by the dual-cavity Helmholtz resonator structure, the three-cavity structure, and the four-cavity structure reveals that the larger the cavity volume, the higher the corresponding peak amplitude.

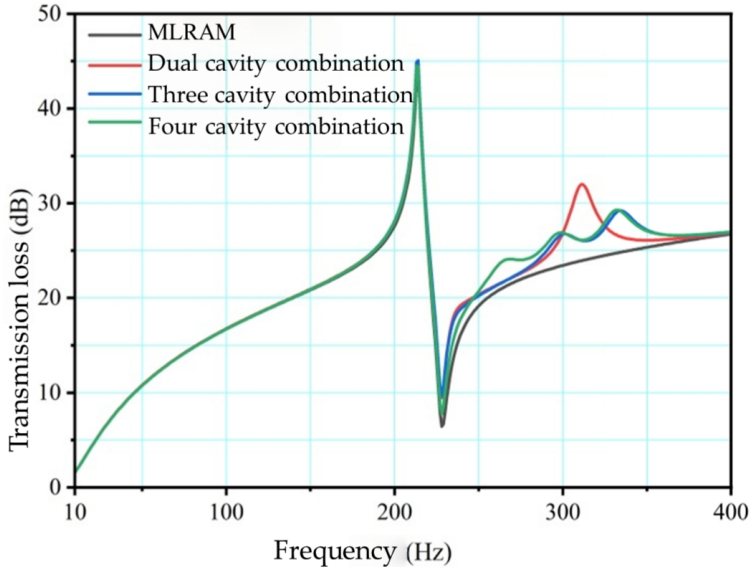

Figure 24. Influence of cavity quantity on sound insulation performance.

3.4.3. Incident angle

The angles of incidence were set to 0°, 30°, 45°, and 60°, respectively, and the calculated sound insulation characteristic curves of the metamaterial composite structure are shown in **Figure 25**. With the increase in the angle of incidence, the sound insulation curves shift downward, the amplitude of the sound insulation peaks increases, the amplitude of the sound insulation valleys decreases, and the overall STL of the composite structure decreases accordingly.

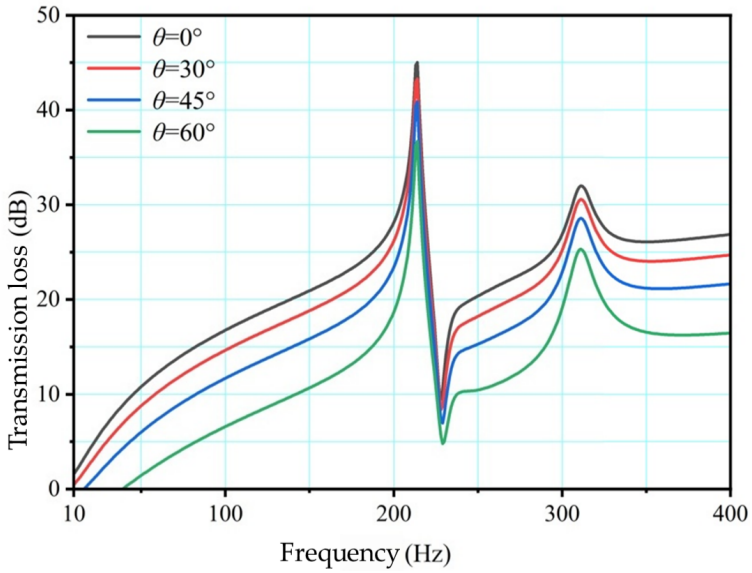

Figure 25. Influence of incident angle on sound insulation performance.

3.5. Optimization design of metamaterial composite structure

By optimizing geometric parameters of Helmholtz resonators to align sub-cavity resonance frequencies near MLRAM's sound insulation valley, three optimized composite structures were designed as shown in **Figure 26**.

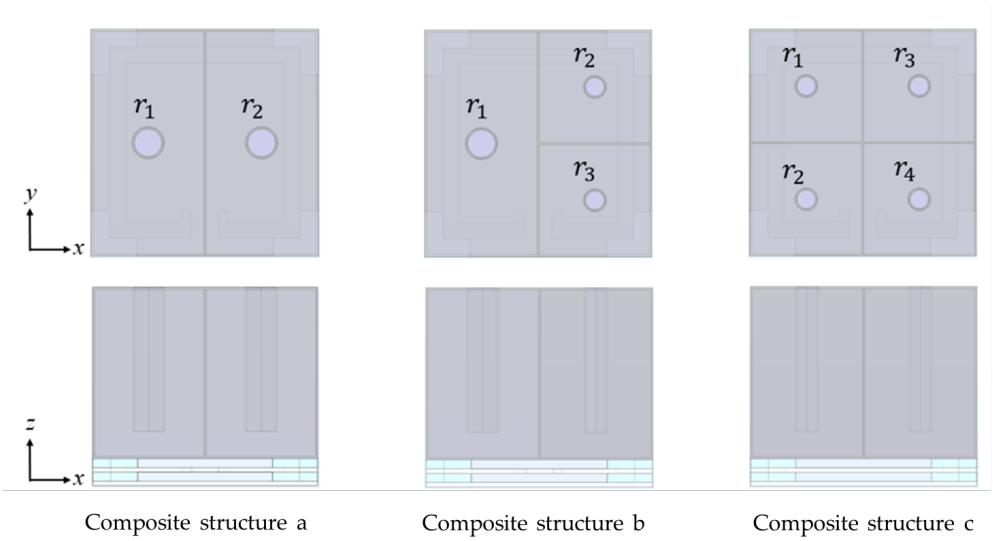

Figure 26. Three optimized composite structures.

The calculated sound insulation curves in **Figure 27** demonstrate that all three optimized structures significantly improve the loss at the trough compared to MLRAM while concurrently enhancing insulation peaks.

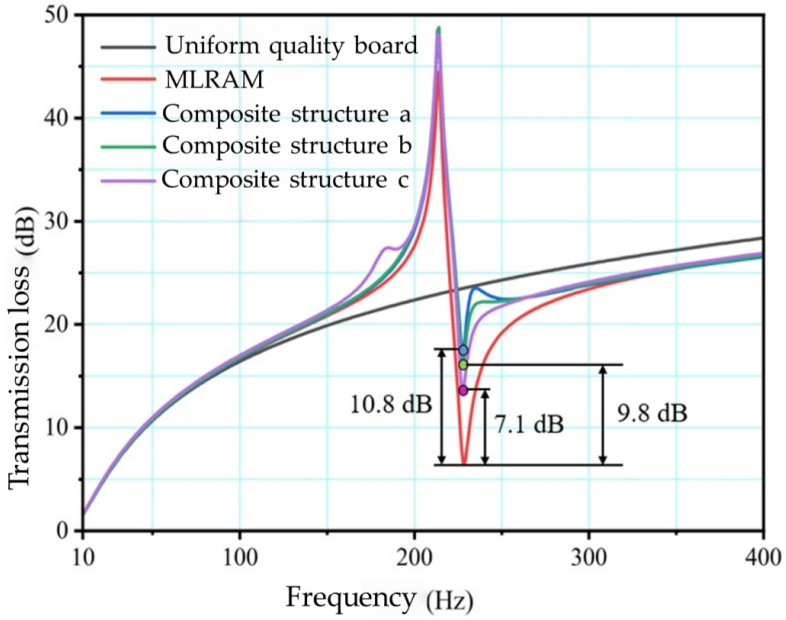

Figure 27. Sound insulation curves of optimized composite structures.

Regarding average sound insulation loss, Structure c exhibits optimal performance while Structure b demonstrates the best comprehensive performance. As shown in **Table 2**, through optimization, all three designs effectively mitigate MLRAM's insulation trough limitation, with dual-cavity Structure a delivering the most significant trough enhancement. These results fully validate the advantage of Helmholtz resonators

in boosting metamaterial sound insulation, providing critical references for subsequent research. The key to performance enhancement lies in the optimized structure, which forms an acoustic energy trap at the sound insulation valley through the coupling of Helmholtz resonance and local resonance, thereby converting propagating waves into localized fields.

Table 2. Comparison of sound insulation performance at trough frequency and average values.

Structure type	Sound insulation loss at trough frequency (dB)	Trough improvement (dB)	Average sound insulation loss (dB)
Equal-mass homogeneous plate	/	/	20.7
MLRAM	6.4	/	20.0
Original composite structure	9.4	3.0	21.0
Composite Structure a	17.2	10.8	21.0
Composite Structure b	16.2	9.8	21.1
Composite Structure c	13.5	7.1	21.2

4. Conclusion

This study successfully designed, fabricated, and evaluated a composite metamaterial structure that integrates MLRAM with dual-cavity Helmholtz resonators to achieve enhanced low-frequency sound insulation. The main conclusions drawn from this work are as follows:

(1) Characterization of MLRAM: The MLRAM structure exhibits a distinctive peak-valley sound insulation characteristic. It produces a pronounced insulation peak (44.5 dB) within its bandgap (around 214 Hz), significantly exceeding the performance predicted by the mass law. However, this peak is inherently followed by a sharp insulation valley (6.4 dB at 228 Hz), which severely limits its overall effectiveness.

(2) Mechanism of Helmholtz Resonators: The dual-cavity Helmholtz resonator operates through a well-defined resonance mechanism, where acoustic energy is intensely concentrated and dissipated within the neck regions. This results in simultaneous sound absorption peaks ($\alpha > 0.99$) and sound insulation peaks at its resonant frequencies (236 Hz and 316 Hz), demonstrating its dual functionality.

(3) Synergistic Performance of Composite Structure: The integration of the Helmholtz resonator with the MLRAM creates a synergistic effect. The resonant dissipation of the Helmholtz resonator actively compensates for the weak insulation region of the MLRAM. The composite structure elevates the original insulation valley by 3.0 dB and introduces a new, substantial insulation peak (32.0 dB), leading to a more balanced and superior average sound transmission loss (21.0 dB) compared to the homogeneous plate and the standalone MLRAM.

(4) Design Flexibility and Optimization: The resonance frequencies of the composite structure can be effectively tuned by modifying key geometric parameters, such as the neck diameter and length. Furthermore, strategies like increasing the number of resonator cavities offer a pathway to broaden the effective insulation bandwidth. The optimization process confirms that the “valley compensation” effect can be significantly enhanced, with improvements of up to 10.8 dB demonstrated,

highlighting the design flexibility and potential for performance tailoring.

Author contributions: Conceptualization, WZ and SJ; methodology, WZ; software, SJ and XZ; validation, SJ and XZ; formal analysis, WZ; investigation, SJ and XZ; resources, LZ and CZ; data curation, WZ; writing—original draft preparation, LZ; writing—review and editing, WZ, LZ and CZ; visualization, XZ; supervision, CZ; project administration, CZ; funding acquisition, CZ. All authors have read and agreed to the published version of the manuscript.

Funding: This research was funded by CRRC Corporation Limited, grant number 2024CCB224. The APC was funded by CRRC Corporation Limited.

Institutional review board statement: Not applicable.

Informed consent statement: Not applicable.

Data availability statement: Data will be made available on request.

Acknowledgment: The authors thank the CRRC Corporation Limited.

Conflict of Interest: The authors declare no conflict of interest.

References

1. Thompson DJ, Hemsworth B, Vincent N. Experimental validation of the TWINS prediction program for rolling noise, part 1: Description of the model and method. Journal of Sound and Vibration. 1996; 193(1): 123–135.
2. Feng T, Wang YH, Wang J, et al. Progress in research and application of structural acoustic metamaterials. Journal of Vibration and Shock. 2021; 40(20): 150–157. (in Chinese)
3. Liu ZY, Chan CT, Sheng P. Analytic model of phononic crystals with local resonances. Physical Review B. 2005; 71(1): 014103.
4. Fang N, Xi DJ, Xu JY, et al. Ultrasonic metamaterials with negative modulus. Nature Materials. 2006; 5: 452–456.
5. Deng K, Ding YQ, He ZJ, et al. Graded negative index lens with designable focal length by phononic crystal. Journal of Physics D: Applied Physics. 2009; 42(18): 185505.
6. Wang G, Wen XS, Wen JH, et al. Quasi-one-dimensional periodic structure with locally resonant band gap. Journal of Applied Mechanics. 2006; 73(1): 167–170.
7. Janssen S, Van Belle L, de Melo Filho NGR, et al. Improving the noise insulation performance of vibro-acoustic metamaterial panels through multi-resonant design. Applied Acoustics. 2023; 213: 109622.
8. Oudich M, Li Y, Assouar MB, et al. A sonic band gap based on locally resonant phononic plates with stubs. New Journal of Physics. 2010; 12(8): 083049.
9. Oudich M, Senesi M, Assouar MB, et al. Experimental evidence of locally resonant sonic band gap in two-dimensional phononic stubbed plates. Physical Review B. 2011; 84(16): 165136.
10. Xiao Y, Wen JH, Wen XS. Sound transmission loss of metamaterial-based thin plates with multiple subwavelength arrays of attached resonators. Journal of Sound and Vibration. 2012; 331(25): 5408–5423.
11. Ho KM, Cheng CK, Yang Z, et al. Broadband locally resonant sonic shields. Applied Physics Letters. 2003; 83(26): 5566–5568.
12. Naify CJ, Chang CM, McKnight G, et al. Transmission loss of membrane-type acoustic metamaterials with coaxial ring masses. Journal of Applied Physics. 2011; 110(12): 124903.
13. Naify CJ, Chang CM, McKnight G, et al. Scaling of membrane-type locally resonant acoustic metamaterial arrays. Journal of the Acoustical Society of America. 2012; 132: 2784–2792.
14. Zhang YG, Wen JH, Zhao HG, et al. Sound insulation property of membrane-type acoustic metamaterials carrying different masses at adjacent cells. Journal of Applied Physics. 2013; 114(6): 063515.
15. Wang XP, Chen YY, Zhou GJ, et al. Synergetic coupling large-scale plate-type acoustic metamaterial panel for broadband sound insulation. Journal of Sound and Vibration. 2019; 459: 114867.

16. Ingard U. On the radiation of sound into a circular tube with an application to resonators. Journal of the Acoustical Society of America. 1948; 20(5): 665–682.
17. Selamet A, Lee I. Helmholtz resonator with extended neck. Journal of the Acoustical Society of America. 2003; 113(4): 1975–1985.
18. Zhang WT, Xin FX. Broadband low-frequency sound absorption via Helmholtz resonators with porous material lining. Journal of Sound and Vibration. 2024; 578: 118330.
19. Sun P, Xu SQ, Wang XL, et al. Sound absorption of space-coiled metamaterials with soft walls. International Journal of Mechanical Sciences. 2024; 261: 108696.
20. Bi SH, Wang ES, Shen XM, et al. Enhancement of sound absorption performance of Helmholtz resonators by space division and chamber grouping. Applied Acoustics. 2023; 207: 109352.
21. Li HM, Wu JW, Yan SL, et al. Design and study of broadband sound absorbers with partition based on micro-perforated panel and Helmholtz resonator. Applied Acoustics. 2023; 205: 109262.
22. Yamamoto T. Acoustic metamaterial plate embedded with Helmholtz resonators for extraordinary sound transmission loss. Journal of Applied Physics. 2018; 123(21): 215110.
23. Laly Z, Mechefske C, Ghinet S, et al. Sound attenuation analysis of a honeycomb structure with extended necks. In: Proceedings of the 2023 International Congress on Noise Control Engineering; 20–23 August 2023; Tokyo, Japan.
24. Langfeldt F, Khatokar AJ, Gleine W. Plate-type acoustic metamaterials with integrated Helmholtz resonators. Applied Acoustics. 2022; 199: 109019.
25. Gu JT, Tang YH, Wang XL, et al. Laminated plate-type acoustic metamaterials with Willis coupling effects for broadband low-frequency sound insulation. Composite Structures. 2022; 292: 115689.
26. Yang XH, Kang YZ, Xie XX, et al. Multilayer coupled plate-type acoustic metamaterials for low-frequency broadband sound insulation. Applied Acoustics. 2023; 209: 109399.